Title

A summary of the BARREL campaigns: Technique for studying electron precipitation.

Journal

Journal of geophysical research. Space physics, 120(6)

ISSN

2169-9380

Authors

Woodger, LA
Halford, AJ
Millan, RM
et al.

Publication Date

2015-06-01

DOI

10.1002/2014ja020874

Peer reviewed

AGU PUBLICATIONS

JGR

Journal of Geophysical Research: Space Physics

TECHNICAL REPORTS: METHODS

10.1002/2014JA020874

Special Section:
New perspectives on Earth's radiation belt regions from the prime mission of the Van Allen Probes

Key Points:
- BARREL observed electron precipitation over wide range of energy and timescales
- Precipitating electron distribution is determined using spectroscopy for 19 January 2013 event
- BARREL timing data has accuracy within sampling interval of 0.05 s

Correspondence to:
L. A. Woodger,
Leslie.Woodger@dartmouth.edu

Citation:
Woodger, L. A., A. J. Halford, R. M. Millan, M. P. McCarthy, D. M. Smith, G. S. Bowers, J. G. Sample, B. R. Anderson, and X. Liang (2015), A summary of the BARREL campaigns: Technique for studying electron precipitation, *J. Geophys. Res. Space Physics*, *120*, 4922–4935, doi:10.1002/2014JA020874.

Received 25 NOV 2014
Accepted 13 MAY 2015
Accepted article online 15 MAY 2015
Published online 10 JUN 2015

A summary of the BARREL campaigns: Technique for studying electron precipitation

L. A. Woodger[1], A. J. Halford[1], R. M. Millan[1], M. P. McCarthy[2], D. M. Smith[3], G. S. Bowers[3], J. G. Sample[4], B. R. Anderson[1], and X. Liang[3]

[1]Department of Physics and Astronomy, Dartmouth College, Hanover, New Hampshire, USA, [2]Department of Earth and Space Sciences, University of Washington, Seattle, Washington, USA, [3]SCIPP, University of California at Santa Cruz, Santa Cruz, California, USA, [4]Space Sciences Laboratory, University of California at Berkeley, Berkeley, California, USA

Abstract The Balloon Array for Radiation belt Relativistic Electron Losses (BARREL) studies the loss of energetic electrons from Earth's radiation belts. BARREL's array of slowly drifting balloon payloads was designed to capitalize on magnetic conjunctions with NASA's Van Allen Probes. Two campaigns were conducted from Antarctica in 2013 and 2014. During the first campaign in January and February of 2013, there were three moderate geomagnetic storms with $SYM\text{-}H_{min} < -40$ nT. Similarly, two minor geomagnetic storms occurred during the second campaign, starting in December of 2013 and continuing on into February of 2014. Throughout the two campaigns, BARREL observed electron precipitation over a wide range of energies and exhibiting temporal structure from hundreds of milliseconds to hours. Relativistic electron precipitation was observed in the dusk to midnight sector, and microburst precipitation was primarily observed near dawn. In this paper we review the two BARREL science campaigns and discuss the data products and analysis techniques as applied to relativistic electron precipitation observed on 19 January 2013.

1. Introduction

It is well known that the particle fluxes in the radiation belts are highly variable due to the continuous interplay between acceleration and loss processes which occur throughout the trapping region [*Reeves et al.*, 2003]. Radiation belt electrons also play a critical space weather role. For example, electrons can damage satellites in orbit [e.g., *Clilverd et al.*, 2012; *Baker*, 1996], and when they precipitate into the upper atmosphere, can affect the production of NO_x leading to ozone destruction [*Clilverd et al.*, 2009; *Callis et al.*, 1996]. Thus, atmospheric loss of radiation belt electrons has been an increasingly important area of focus in the space physics research community.

Particle loss from the radiation belts can be described as a decrease in flux when those particles have not simply been displaced due to adiabatic effects, but rather permanently removed such that phase space density remains low even after the magnetic field has recovered [e.g., *Green et al.*, 2004]. The two main processes that cause particle loss in the radiation belts are magnetopause loss, when particle trajectories intersect the magnetopause [e.g., *Hudson et al.*, 2014; *Turner et al.*, 2012; *Ukhorskiy et al.*, 2006], and pitch angle scattering into the atmosphere through wave-particle interaction [e.g., *Thorne*, 2010; *Millan et al.*, 2007]. A spectrum of plasma wave frequencies ranging from ultralow frequency (ULF), (*f*~mHz–Hz), to very low frequency (VLF), (*f*~kHz), and higher has been observed and characterized in the magnetosphere [*Millan and Thorne*, 2007; *Anderson et al.*, 1992; *Sazhin and Hayakawa*, 1992]. Theory suggests that these waves can pitch angle scatter electrons with relativistic energies [*Meredith et al.*, 2003; *Lorentzen et al.*, 2001; *O'Brien et al.*, 2004; *Blake et al.*, 1996; *Imhof et al.*, 1992; *Thorne and Kennel*, 1971]

Many studies have characterized the various energies and temporal features of electron precipitation in order to ascertain the driving precipitation mechanism. The first electron precipitation with temporal features of ~0.25 s, microburst precipitation, was observed by balloon-borne instrumentation during the early 1960s [*Anderson and Milton*, 1964]. The microbursts were attributed to electron precipitation at energies near 100 keV and had a preferential local time occurrence in the dayside magnetosphere. The first relativistic electron microbursts ($E > 1$ MeV) were observed by instrumentation on board S81-1, a low Earth-orbiting satellite [*Imhof et al.*, 1992]. Comparison between low-energy microbursts and relativistic microbursts show observable differences between the two phenomena. Relativistic microburst events occur over a narrow latitude region mostly in the nightside magnetosphere, at higher *L* values with low fluxes [*Imhof et al.*, 1992;

Blake et al., 1996]. The softer microbursts observed primarily on the dayside suggests resonance with VLF chorus waves as the precipitation mechanism. *Lorentzen et al.* [2001] suggested that whistler mode waves are also the precipitation mechanism for relativistic electron microbursts observed by the SAMPEX satellite as when relativistic microburst precipitation was observed on the dayside magnetosphere it was accompanied by more intense lower-energy microbursts.

The first balloon-borne observation of duskside relativistic electron precipitation with temporal features >1 s occurred over Kiruna, Sweden in 1996. The precipitation lasted about 20 min and displayed temporal modulation on the order of ULF time scales [*Foat et al.*, 1998]. The MAXIS balloon experiment followed in January of 2000 and showed that duskside precipitation may account for significant loss of relativistic electrons [*Millan et al.*, 2010, 2007, 2002]. A more recent study using SAMPEX data showed that precipitation, generally well fit by an exponential energy distribution with *e*-folding energy >500 keV, occurred primarily in the dusk-to-midnight sector [*Comess et al.*, 2013]. This type of precipitation was historically identified as "spikes of precipitating electrons" by *Brown and Stone* [1972]. *Imhof et al.* [1986] further showed that precipitating electron "spikes" occur with proton (E>30 keV) precipitation predominantly along the duskside plasmapause. *Blake et al.* [1996] described the "spikey" electron precipitation reported by *Brown and Stone* [1972] and *Imhof et al.* [1986] as "band" precipitation due to its distinguishable temporal characteristics as compared to microburst precipitation. Several studies have proposed electromagnetic ion cyclotron (EMIC) waves as the precipitation mechanism causing duskside relativistic electron precipitation [*Usanova et al.*, 2014; *Millan et al.*, 2002; *Lorentzen et al.*, 2000; *Foat et al.*, 1998]. However, without simultaneous in situ measurements of waves and local precipitating particles, this hypothesis has been difficult to quantitatively test.

The Balloon Array for Radiation belt Relativistic Electron Losses (BARREL), a mission of opportunity in collaboration with NASA's Van Allen Probes, was designed to observe and further investigate energetic electron precipitation in order to characterize atmospheric electron loss and quantitatively test wave-particle interaction theories [*Millan et al.*, 2013; *Millan and BARREL Team*, 2011]. BARREL is an array of stratospheric balloons that observes bremsstrahlung X-rays from radiation belt electrons precipitating into Earth's atmosphere. Two campaigns were conducted from the Antarctic South African and British stations, SANAE and Halley VI, during the southern hemisphere summers of 2013 and 2014. These launch locations offer many opportunities for conjunctions with the twin Van Allen Probes. The Van Allen Probes have a highly elliptical (perigee at ~600 km and apogee at 5.8 R_E) 9 h orbit at a 10° inclination [*Mauk et al.*, 2013]. BARREL measurements combined with the conjugate Van Allen Probe observations of both waves and particles provide a unique opportunity to study the physics of wave-particle interactions.

This paper provides an overview of the BARREL Antarctic balloon campaigns. We describe the wide range of precipitation observed, summarize some science highlights of the mission, and describe the data and analysis techniques as applied to a precipitation event that occurred on 19 January 2013. Section 2 briefly describes the BARREL payload and resulting data. Also, in this section we describe the magnetic coverage of the observations, conjunctions with the Van Allen Probe satellites, and a few example studies that incorporate both BARREL and satellite observations. Sections 2.2 and 2.3 introduce the selected diverse BARREL X-ray observations which are further analyzed in sections 3.1 and 3.2. The analyzed events are further discussed in section 4.0 along with some concluding remarks.

2. The BARREL Mission Summary

BARREL was designed to study the loss of radiation belt particles to the upper atmosphere. As radiation belt electrons precipitate, they suffer ionization losses and produce bremsstrahlung X-rays with energy less than the precipitating electron energy as they interact with the atmosphere. The photons are eventually absorbed by the atmosphere before reaching the ground; thus, BARREL makes science measurements at altitudes greater than the nominal altitude of 27 km.

Each payload carried a 3″×3″ NaI spectrometer which detects 20 keV–10 MeV X-rays produced by precipitating electrons from the radiation belts [*Millan et al.*, 2013]. Three X-ray data products, fast spectra (FSPC), medium spectra (MSPC), and slow spectra (SSPC), are available with different energy and time resolution described in Table 1 and shown in Figure 1 and described in *Millan et al.* [2013]. The different time

Table 1. BARREL X-ray Data Sets

X-ray Data Product	Energy Range (keV) (Nominal)	Channels	Time Resolution
Fast spectra (FSPC) Campaign 1	FSPC1 = 25–180 FSPC2 = 180–550 FSPC3 = 550–840 FSPC4 = 840–1500	4	50 ms
Fast spectra (FSPC) Campaign 2	FSPC1a = 25–48 FSPC1b = 48–95 FSPC1c = 95–180 FSPC2 = 180–550 FSPC3 = 550–840 FSPC4 = 840–1500	6	50 ms
Medium spectra (MSPC)	100–4,000	48	4 s
Slow spectra (SSPC)	25–10,000	256	32 s

scales and energy resolution allow for observations of a wide range of precipitation events in both energy and time. Figure 1 (top) is a spectrogram plot of BARREL slow spectra observed on 7–8 January 2014 discussed in *Halford et al.* [2015]. The figure shows various features in the X-ray data that are from both electron precipitation and other sources [*Halford et al.*, 2015]. For example, the enhanced region near the center of the plot which extends across a broad energy range is due to gamma rays from atmospheric nuclei excited by a solar energetic proton (SEP) event. A small intense peak from a solar flare is observed in the data during the evening of 7 January 2014. The 511 keV line from electron-positron annihilation is also a feature that can be easily observed. The spectrum's wavy lower margin reflects a temperature and payload-dependent low-energy cutoff. Electronic noise is often prominent in the lowest-energy channels and is responsible for the sinuous orange feature near 40 keV. Figure 1 (bottom) shows the fast spectral data observed over the same 2 days from three different balloon payloads. In this plot the features such as the relativistic electron precipitation (REP) event, SEP event, and solar flare are also observed. Another type of nonelectron-precipitation event that was observed by BARREL and is not shown in Figure 1 is cosmic gamma ray bursts (GRBs). Section 2.3 below discusses one particular GRB observed on 21 January 2013.

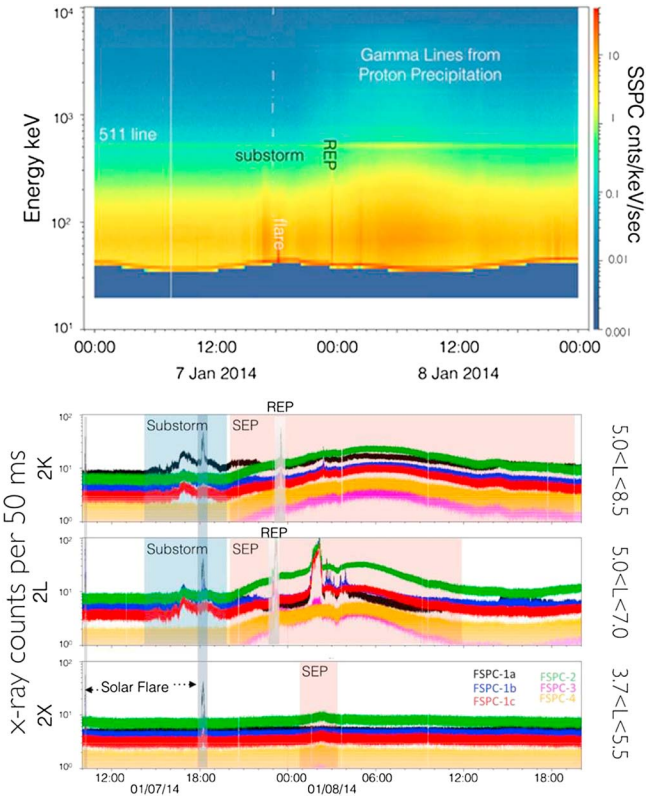

Figure 1. X-ray products from the BARREL 2013–2014 campaigns. (top) Slow spectra data during the 2014 campaign. (bottom) Fast spectra data from three BARREL balloons during the same 2 days shown in the top plot.

Each BARREL balloon also carried a triaxis fluxgate magnetometer with a sampling rate of 4 Hz. This instrumentation is capable of fully sampling ULF (Pc1–Pc5) frequencies at or below the 2 Hz Nyquist frequency; however, these low-amplitude waves (on the order of nanotesla) can be challenging to detect due to the strong signatures (on the order of microtesla) from the balloon payload's random motion. The magnetic field magnitude observed by payload 1K on 8 January 2014 is shown in Figure 2. Here the data contain some small-amplitude contamination from payload motion but overall agree well with International Geophysical Reference Field (IGRF) and 1989 Tsyganenko (T89) magnetic field models.

Data from the Global Positioning System (GPS) on board the payloads provide accurate timing and position data. The position data can be used to map the locations of the balloons out into the magnetosphere. The timing data are used to increase the accuracy of the timing information on X-ray events and

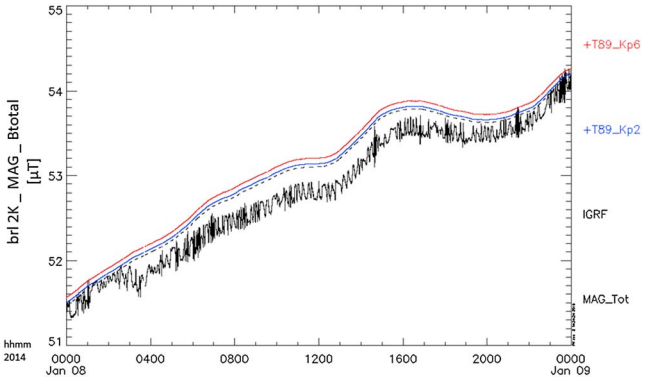

Figure 2. Total magnetic field observations from BARREL payload 2K as compared to magnetic field models IGRF and T89.

will be discussed further in section 3.2. Further details on instrumentation have been reported by *Millan et al.* [2013].

Each BARREL campaign consisted of 20 payloads divided between two launch locations in Antarctica, SANAE IV (L~4, campaign 1: 13 payloads, campaign 2: 10 payloads) and Halley VI (L~4.5, campaign 1: 7 payloads, campaign 2: 10 payloads). The average duration of flight for the payloads was ~12 days with maximum flight duration of 38 days, payload 1I in 2013. Throughout the campaign an average of six balloons were aloft at any given time. The first payload was launched on 1 January 2013 with the last payload of the first campaign terminated on 16 February 2013. The second campaign started with its first launch on 27 December 2013, and the last payload was terminated on 11 February 2014. With multiple payloads aloft at any given time, an array of balloons which covered a range of L and magnetic local time (MLT) was established. The launch sites were chosen for their geomagnetic position which maximizes the amount of time spent in regions that magnetically map to the radiation belts. The balloons drift at speeds of 10–20 knots as they circumnavigate the Antarctic continent and sweep through ~24 h of MLT each day. Due to the tilt of the Earth's magnetic field, the balloon payloads slowly drift westward, to regions which map to higher L values and eventually through the polar cap. Figure 3 (top) shows the cumulative L and MLT coverage of the BARREL balloons during the two campaigns as calculated using the T89c model with $Kp = 2$.

As a NASA Living with a Star Geospace Mission of Opportunity in support of the Van Allen Probes mission, conjunctions between the established array of BARREL balloons and Van Allen satellites during both 2013 and 2014 campaigns were closely monitored (Figure 3, bottom). Throughout both Antarctic campaigns, daily telecons were supported by BARREL and Van Allen Probe's instrument team personnel. High sampling rate burst data were collected and telemetered by the Electric Field Wave team for time periods of good satellite and balloon conjunctions with interesting solar activity. Personnel from other Van Allen instrumentation teams such as Electric and Magnetic Field Instrument Suite and Integrated Science; Radiation Belt Storm Probes Ion Composition Experiment; and Energetic Particle, Composition, and Thermal Plasma Suite (ECT) also participated in these daily telecons and coordinated their instrument operations and telemetry. Over the course of the BARREL field campaigns there were also many other conjunctions between the BARREL balloons and ground-based magnetometers, riometers, and satellites including two CubeSat missions, Colorado Student Space Weather Experiment (CSSWE), and Firebird [e.g., *Blum et al.*, 2013].

The collective observations of BARREL electron precipitation and conjunctive satellite and ground-based observations allow for collaborative studies of the in situ particle populations, wave observations, and measurements of local plasma parameters that likely contributed to the observed precipitation events. A recent study by *Li et al.* [2014] used GOES and Van Allen Probe observations to model the pitch angle diffusion between resonant relativistic electrons and observed EMIC waves. The results of this model showed good agreement with the precipitation observed by one of the BARREL balloons. Another study by Breneman et al. [Global coherence scale modulation of radiation belt electron loss from plasmaspheric hiss, submitted to Nature, 2015] investigates correlated temporal profiles between plasmaspheric hiss, observed by Van Allen Probes, and electron precipitation as observed by the BARREL balloons.

Throughout both campaigns there were many well-spaced time periods with geomagnetic activity which allowed for the interesting and isolated electron precipitation events to be observed. Figure 4 shows the solar wind conditions as extracted from NASA/Goddard Space Flight Center (GSFC)'s OMNI data set through OMNIWeb during each balloon campaign. During the first campaign, the solar wind speed rarely

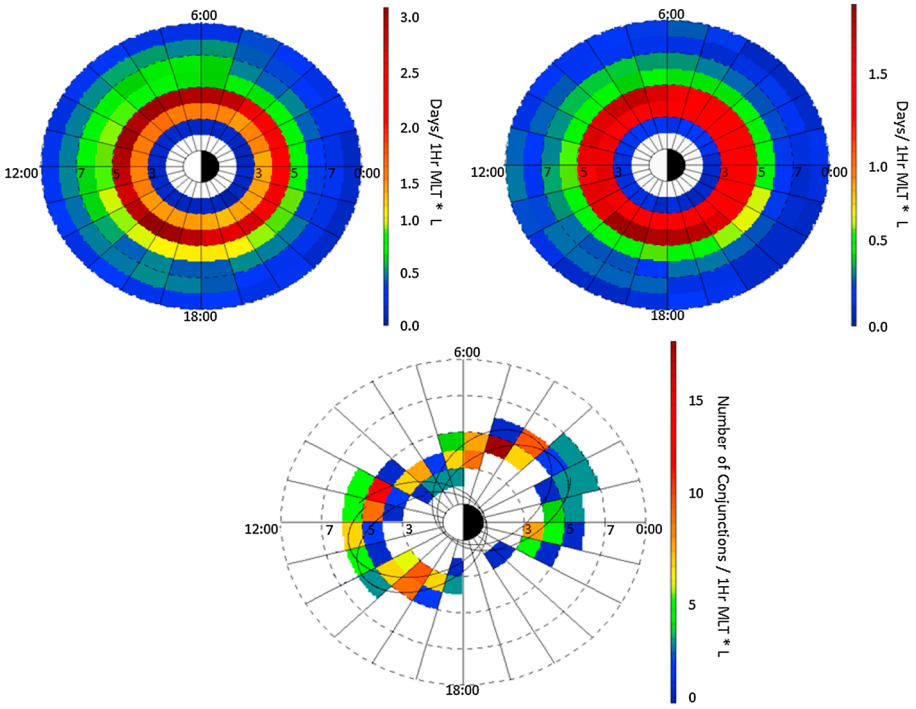

Figure 3. BARREL *L* value and MLT coverage during (top left) 2013 campaign and (top right) 2014 campaign. (bottom) The number of BARREL and Van Allen Probes conjunctions per 1 h MLT and 1 *L* shell during the 2013 and 2014 BARREL field campaign. Superimposed on the plot is sample Van Allen Probe orbits for January and February of 2013 and 2014. Locations are mapped using the T89c model.

exceeded 500 km/s; however, three moderate storms occurred with a *SYM-H*$_{min}$ < -40 nT. The second campaign had multiple high-speed stream and coronal mass ejection events. However, B_z stayed predominately northward, thus producing minor storms with *SYM-H*$_{min}$ > -40 nT. Observations of temporal features in the X-ray data ranged from tens of milliseconds to tens of minutes [*Blum et al.*, 2013]. Time scales more commonly associated with drift echoes (Halford, private communication) were also observed. Spatial observations varied from a single payload detecting an event to multiple or even all aloft payloads observing the same structures. BARREL observations during selected events are presented in sections 2.1, 2.2, and 2.3 with spectral analysis and timing considerations discussed in sections 3.1 and 3.2.

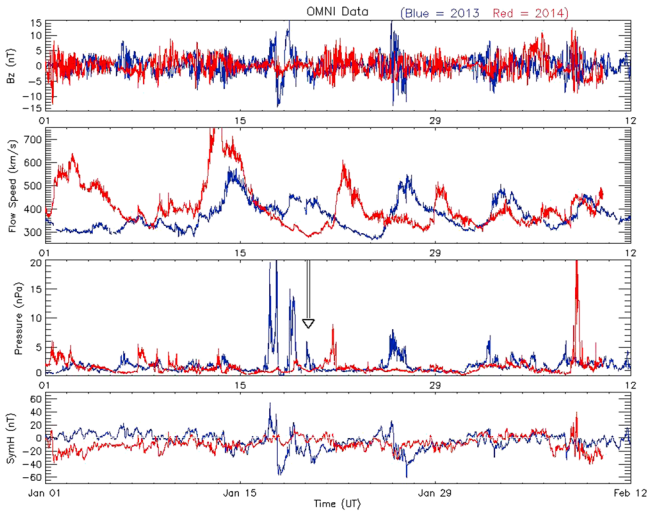

Figure 4. OMNI solar wind observations during the two BARREL campaigns, 2013 (blue) and 2014 (red). The black arrow points to the increase in dynamic pressure (blue curve) associated with the 19 January 2013 analysis described in sections 2.2 and 3.1.

2.1. BARREL Soft Electron Precipitation Observation: 26 January 2013

A small geomagnetic storm started late on 25 January 2013 as interplanetary field component B_z turned southward and predominantly stayed southward for most of the following day. During this time period BARREL observed electron precipitation with a variety of

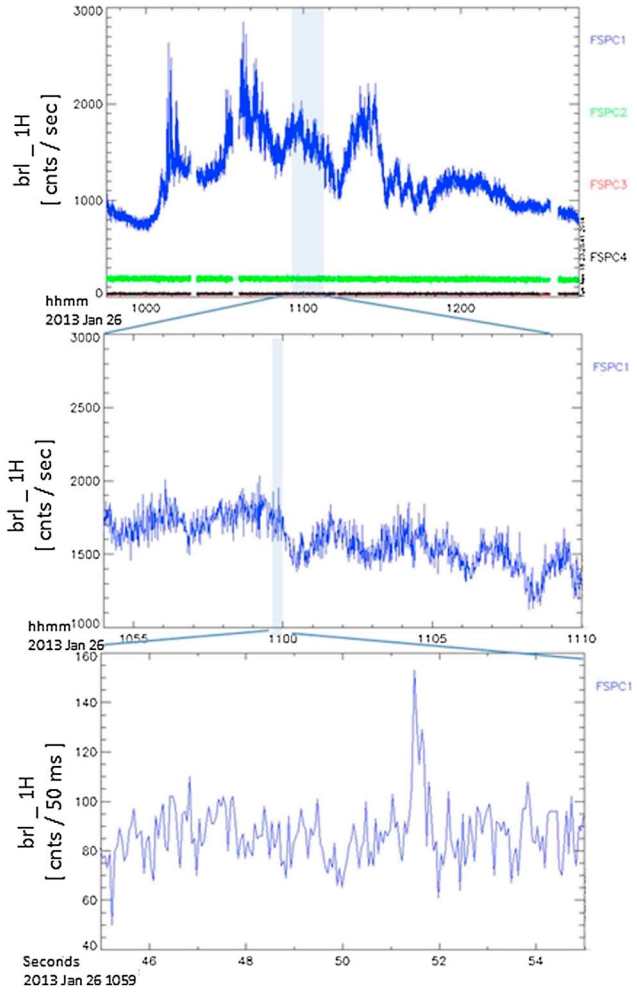

Figure 5. Electron precipitation observed by BARREL payload 1H on 26 January 2013. (top) FSPC data at 1 s time resolution and energy range from 20 keV to 1.5 MeV over four energy channels. (middle) FSPC 1 data at 1 s time resolution. (bottom) Microburst precipitation in FSPC 1 data at full time resolution.

temporal features. BARREL fast spectral X-ray count rate data (FSPC) in Figure 5 show observations from payload 1H on 26 January 2013. Figure 5 (top) shows all four energy channels where the counts over 1 s of the 50 ms data have been summed together. The individual higher-energy channels FSPC 2, FSPC 3, and FSPC 4 did not show observable increases in count rates suggesting that the precipitation was due to electrons with energies $<$200 keV. Since the FSPC data are not background subtracted, the extremely hard cosmic ray background can sometimes dominate the X-ray counts at higher energies during weak precipitation events. Therefore, in order to accurately determine the energies of the precipitating electron population, a spectral analysis should be performed. Periodic variations in the X-ray counts lasting on the order of tens of minutes were observed as shown in Figure 5 (top). This periodicity is approximately the drift time scale of 300 keV radiation belt electrons. A subset of the data has been expanded in Figure 5 (middle) with only the lowest-energy channel, FSPC 1, presented. The X-ray count rate is observed to have periodicity on the order of the upper limit for Pc5 ULF time scales, ~2.5 min (Figure 5, middle). Microbursts can be observed on a much shorter time scale, as increased count rate above background on the order of hundreds of milliseconds. Microbursts often occur as a series of bursts which aids in identifying this type of precipitation in satellite data as well as balloon data. Through fast Fourier transforms of precipitating flux data, *Comess et al.* [2013] was able to identify microburst precipitation in SAMPEX data. *Rosenberg et al.* [1990] proposed an algorithm for identifying microburst precipitation in balloon data by scanning a 4 s window of low-pass-filtered and mean-subtracted X-ray count rate data for time periods where the count rate exceeded 10 times the square root of the mean for more than 200 ms. Figure 5 (bottom) shows an expanded view of a single microburst identified visually in the X-ray count rate data and observed by BARREL payload 1H plotted in a 10 s time window with full time resolution fast spectral data. Scanning over a longer time period during this event shows microburst electron precipitation throughout the first half of the entire precipitation time period.

2.2. BARREL REP Observation: 19 January 2013

On 19 January 2013 at ~18:45 UT, B_z rotated southward, and a small but abrupt increase in solar wind dynamic pressure was reported in OMNI data. There were six BARREL balloons aloft during this time period which spanned ~8 h in MLT and L values from ~4.5 into the polar cap. Figure 6 shows the L and MLT locations of those BARREL payloads which mapped to closed field lines using the T89c magnetic field model. BARREL payload 1H (L~4.5, MLT~19.5 h) observations are shown in Figure 7. The X-ray data

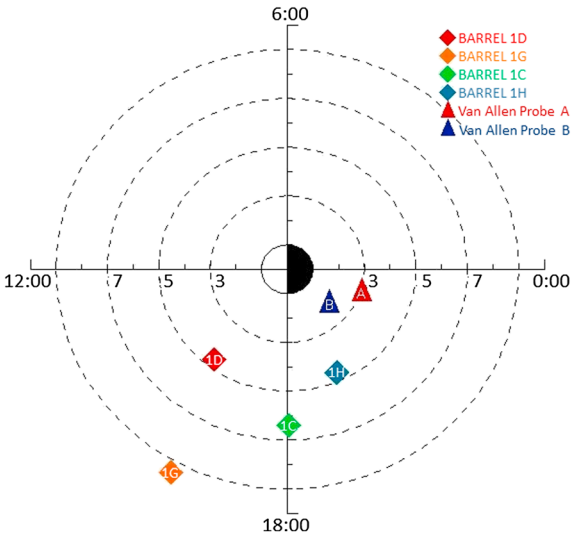

Figure 6. *L* and MLT location of BARREL payloads and Van Allen Probes A and B at 23:20 UT on 19 January 2013. Locations are mapped using the T89c model.

products, fast, medium, and slow spectra (FSPC, MSPC, and SSPC) each offer a slightly different perspective for the same observations. Figure 7 (top) shows the fast spectral data, where large increases in X-ray count rates starting at ~23:08 UT are observed. The increases in the higher-energy channels indicate that this event is from relativistic electron precipitation. The medium spectra are shown in Figure 7 (middle), and the slow spectra are shown in Figure 7 (bottom). The MSPC and SSPC data extend the energy range of the observations to 4 MeV and 10 MeV respectively, although this particular event does not extend to those energies. All three X-ray data products show two events of relativistic electron precipitation, the first lasting ~6 min and the second lasting ~12 min. The second, more intense event starting at 23:18 UT shows modulation over the three peaks with a periodicity (~2.5 min) at the upper edge of the Pc5 ULF wave frequency range. Electron precipitation with ULF wave time scale modulation was observed by payload 1C during a similar time period as payload 1H. However, payload 1C does not see any electron precipitation coincident with the second event observed by payload 1H starting at 23:18 UT. Spectral modeling of payload 1H's second event to determine the flux and energy distribution of the precipitating electrons is investigated in section 3.1. The energy information extracted from the X-ray data contributes to determining the precipitation mechanism of the electrons, and the flux estimate determines if the event has significant impact on the radiation belt particle population.

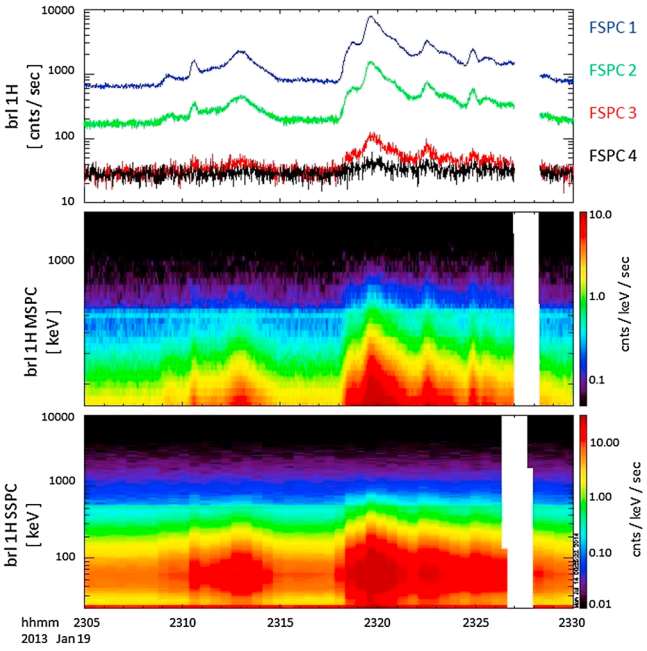

Figure 7. Relativistic electron precipitation observed by BARREL payload 1H on 19 January 2013. (top) Four energy channels of FSPC data at 1 s time resolution, (middle) MSPC data in spectrogram format, and (bottom) SSPC data.

2.3. BARREL Gamma Ray Burst Observation: 21 January 2013

On 21 January 2013, Fermi's Gamma-ray Burst Monitor (GBM) triggered on a gamma ray burst (GRB) identified as GRB130121835 (Figure 8a). Gamma ray bursts are the most energetic phenomena observed [*Piran*, 2004], whose origin remains unclear. The Fermi Gamma-ray Space Telescope was launched in June of 2008. The spacecraft orbit has an altitude of 565 km at ~26° inclination with very low eccentricity (<0.01). The Gamma-ray Burst Monitor consists of 12 NaI scintillators and 2 cylindrical bismuth germanate scintillators and is sensitive to energies from 8 keV to ~40 MeV [*Meegan et al.*, 2009]. The high time resolution (2 μs) GBM data provide gamma ray burst trigger and location information, as well as spectral information of GRBs. The trigger time for the GRB detected on 21 January 2013 was reported at 20:01:59.967. Five of the six BARREL balloons aloft during this time

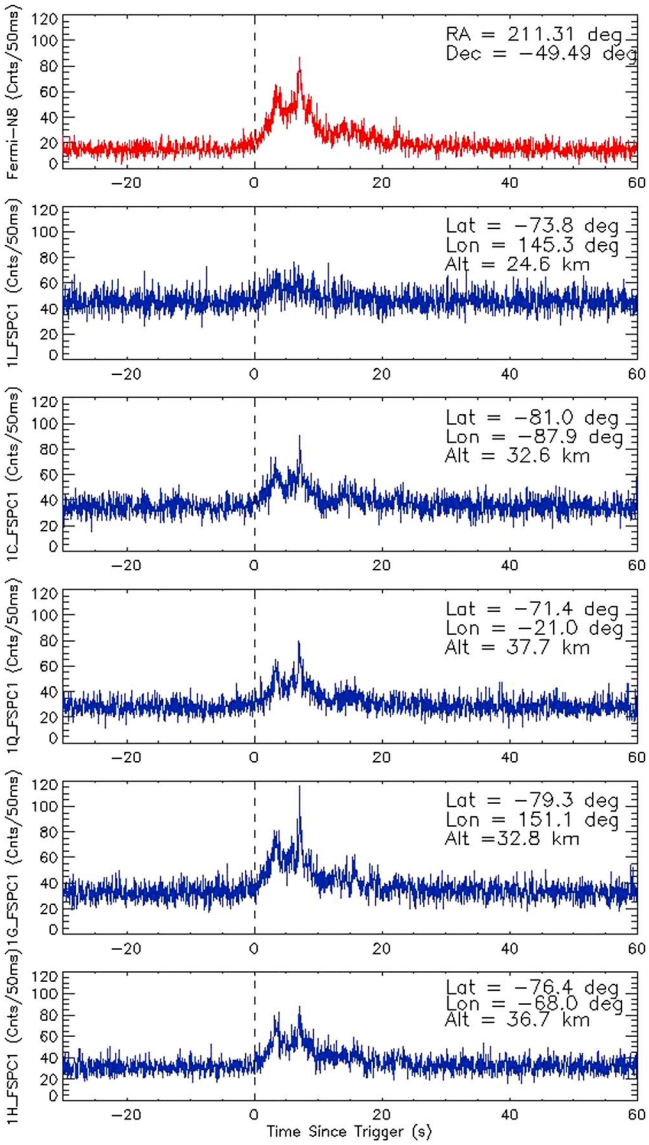

Figure 8. GRB observations on 21 January 2013 (a) Fermi-GBM N8 NaI scintillator X-ray data extracted from Fermi fits file (b–f) BARREL fast spectra data for payloads which observed the GRB triggered on Fermi. The black vertical line marks the trigger time observed by Fermi at 20:01:59.967 UT.

period were in position to observe the GRB as a simultaneous short increase in count rate of the FSPC data (Figure 8). One payload, 1D, did not observe the GRB as its altitude was 19 km at the time of the event and the gamma rays were absorbed in the atmosphere before reaching this payload. Similarly, payload 1I was at a low altitude in comparison to the other BARREL balloons and therefore observed a highly attenuated signal. Payload 1G observed the strongest signal even though it was not at the highest altitude because the right ascension and declination information provided by Fermi GBM observations for this event show the GRB was nearly overhead and the photons did not traverse as much atmosphere to reach the balloon. A satellite such as Fermi with instruments engineered to study such events provides an opportunity to investigate the timing and correlation of events observed by BARREL through simultaneous observations of the GRB. Section 3.2 discusses the timing accuracy of the BARREL data. Confidence in the timing of BARREL 50 ms resolution data allows for the comparison and correlation of observed electron precipitation events between balloon payloads and satellites. For instance based on the timing of events observed by multiple balloons and correlation with satellite observations, competing hypothesis such as wave-particle interaction, drifting precipitating particles, or defined regions of precipitation can be investigated.

3. Data Analysis

3.1. Spectral Analysis: 19 January 2014

The BARREL NaI spectrometer observes bremsstrahlung X-rays from the precipitating electron population. The precipitating electron energy spectrum and flux can be inferred from the background-subtracted medium and slow spectra utilizing a forward folding technique. The forward folding technique is described by *Millan et al.* [2013] but is briefly described here as applied to a specific precipitation event observed by BARREL. Initially, a precipitating electron distribution is assumed. For the second event observed on 19 January 2013 and described in section 2.2 above, we compare results of different modeled input electron distributions. Input distributions are then folded with a response matrix which accounts for the atmospheric and instrument response at given balloon altitude. The result is a model X-ray count spectrum which can then be compared with the BARREL-observed count spectrum.

The response matrix was developed with a two-stage Monte Carlo simulation using GEANT 3. The Monte Carlo simulation includes all relevant physics, most importantly energy loss of the incident electrons through ionization and excitation of air molecules, bremsstrahlung production, and scattering and absorption of the photons in both the atmosphere and instrument.

The first stage of the simulation models the atmospheric response using a scaled model of the atmosphere where atmospheric depth is equivalent to the real polar atmosphere. Electrons are launched at an 85 km altitude with 27 discrete energies spanning the range from 50 keV to 4 MeV. The electrons lose energy and occasionally produce bremsstrahlung X-rays in the mass model of the atmosphere. The energy and zenith angle of both photons and secondary electrons and positrons (of which there are very few) that reach altitudes of 25, 30, 35, and 40 km are recorded. The first generation of the response assumes that the incoming electrons are distributed isotropically in the downward hemisphere, as would be expected for strong pitch angle scattering. A version of the response with mirroring electrons (characteristic of slow pitch angle diffusion) is being generated as of this writing. It is found that the pitch angle distribution of the modeled input electron flux does not greatly affect the spectral shape of the bremsstrahlung photon spectrum.

In the second stage, the output from the stage one atmospheric response is used as an input to determine the instrument response. The simulated photons and secondary electrons are placed on the surface of a sphere surrounding the instrument mass model and projected inward. The zenith angle is preserved, but the azimuth angle and position on the sphere are random. This allows each output particle from stage one to be resampled several times to improve the counting statistics of stage two.

In stage one the particles were captured on a horizontal surface at balloon altitude, but they are being projected onto a spherical surface in stage two. This produces a bias in which nearly horizontal particles are undersampled in stage one. This is corrected by weighting the stage one output particles in stage two by one over the cosine of their zenith angle. The physics dominating the second step of the modeling includes Compton scattering, pair production, and photoelectric absorption in the NaI detector and surrounding passive material.

The result of the two-stage simulation is a collection of 108 measured X-ray responses to incident electrons, coming from 27 electron energies over the 50 keV to 4 MeV range and at four altitudes. Each X-ray response is then fit to a parameterized empirical function that reproduces the simulated spectral shapes. All of the simulation results are thereby reduced to a compact collection of parameter lists.

A response matrix is built from the condensed simulation output that converts a trial electron spectrum into inferred X-ray observations. To build a response matrix, function parameters are interpolated in electron energy onto a standard set of electron energy bins. For each electron energy, the empirical function is evaluated at a set of standard photon energies, 256 for slow spectra and 48 for medium spectra. In order to interpolate to an input electron energy E between two simulated energies, the output (photon) energy spectrum for each of the two simulated responses is stretched or compressed linearly so that both the simulated bremsstrahlung spectra run from zero to E. The values at each now aligned photon energy are interpolated logarithmically to get the final spectrum. The interpolation in altitude is performed next and is a linear interpolation between the spectra for the modeled altitudes above and below the balloon altitude. The product of the response matrix and an electron flux vector gives an inferred X-ray spectrum that is compared with measurements. For instance, by parameterizing a model form for an input electron spectrum, a chi-square minimization can be used to locate optimal parameters for that model.

The spectral analysis technique discussed above is applied by the BARREL spectroscopy code (available through BARREL Data Analysis Software (BDAS) which is incorporated into Space Physics Environment Data Analysis Software (SPEDAS)) to a precipitation event observed on 19 January 2013. We present two electron distributions in Figure 9a to show the capability of the software to model distributions represented by defined peaked function (monoenergetic) as well as observations with a more complicated broad distribution in energy (Magnetic Electron Ion Spectrometer (MagEIS) data). The solid black line in this panel represents a monoenergetic electron distribution represented as a narrow banded top hat function (see Table 2). The dashed line in Figure 9a shows the scaled electron (10 keV–3.5 MeV) fluxes at 172° pitch angle observed by the MagEIS instrument on board Van Allen Probe A. A background-subtracted spectrum is first obtained from the observations using energy bin calibrated level 2 data in order to remove nonelectron precipitation signatures such as cosmic ray noise and the 511 line. Figure 9b

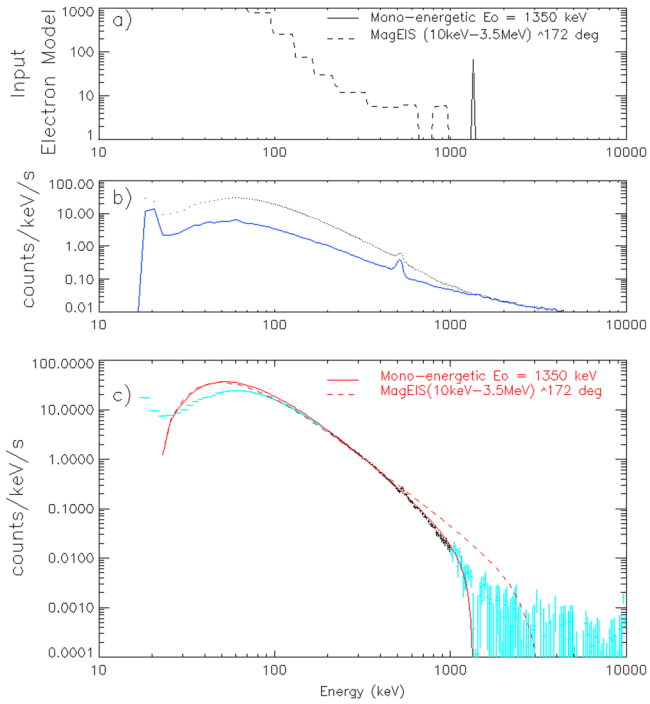

Figure 9. Spectroscopy results for 19 January 2013 REP event. (a) Input electron distribution shapes. (b) BARREL X-ray observed spectrum (black) and background spectrum (blue). (c) BARREL background subtracted X-ray spectrum with error bars (black and blue) and fitted modeled spectra based in input electron distribution (red). The solid red line represents a modeled 1350 keV monoenergetic electron distribution. The dashed red line represents modeled spectrum from MagEIS electron observations at 172° pitch angle for 10 keV–3.5 MeV.

shows in black the observed spectrum between 23:18 UT and 23:26 UT. The blue curve in this plot is the background spectrum obtained by quiet time periods selected before the REP event. The large peak at the lowest energies is a result of noise in the detector near its lower threshold. The 511 keV electron-positron annihilation line is evident in both the observed and background spectra. A good background subtraction will remove almost all of this line since it is due mostly to cosmic ray background and not produced by precipitation except for a few positrons due to pair production from gammas ≫1 MeV. Figure 9c shows in black (the selected energy range for fitting) and cyan (energy ranges outside fitting range) the background subtracted spectrum with error bars (crosses). The error bars are determined from Poisson statistics based on the photon counts in the observed spectra and do not include systematic errors. The energy fit range is selected based upon counting statistics, systematic uncertainty in the background spectrum (high part of the energy range), and systematic uncertainties in the channel-to-energy conversion and response matrix (low part of the energy range). Modeled photon count spectra for the input electron distributions are shown in red in Figure 9c. The resulting modeled photon spectrum for the scaled MagEIS electron spectrum is shown as a dashed red line at Figure 9c. This model is inconsistent with the BARREL observations because it greatly overpredicts X-ray flux from 600 to 1000 keV. The BARREL-observed X-ray spectrum is better modeled using a 1350 ± 50 keV monoenergetic electron distribution (solid red line). This suggests that the precipitating electron distribution is a peaked spectrum resulting from an energy selective precipitation mechanism.

It is important to note how similar the modeled spectra in Figure 9 look at lower to moderate energies, while at the higher energies the individual spectra start to separate. *Berger and Seltzer* [1972] noted and explained this phenomenon in their discussion of the forward folding technique applied to balloon X-ray observations. Therefore, differences between modeled electron spectra are resolved at the high-energy end of the spectrum since low-energy X-rays are more likely to interact with air. Also, a traditional minimum chi-square fit will be dominated by even very small differences at lower energies, where the error bars on the data are very small from Poisson counting statistics. In order to overcome these problems, we restrict fitting to higher energies only.

Table 2. Monoenergetic Electron Distribution Characteristics

Input Electron Model	Format	Fit Parameters
Monoenergetic	$F(E) = A(H(E - 1340\ \text{keV}) - H(E - 1360\ \text{keV}))$	$A = 128\ e/\text{keV cm}^2\ \text{s}$ $E_o = 1350 \pm 50\ \text{keV}$
	$H(x) = \begin{cases} 0, x < 0 \\ 1, x \geq 0 \end{cases}$	

The flux of precipitating monoenergetic electrons can be estimated by integrating the modeled electron spectrum described in Table 2. We estimate a modeled precipitating electron flux

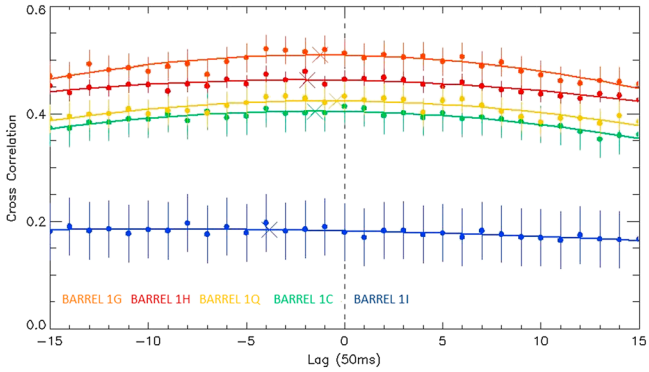

Figure 10. Cross correlation between BARREL payload FSPC data and Fermi GRM N-8 scintillator during GRB observation. Cross correlations are calculated between Fermi and BARREL 1H (red), 1Q (yellow), 1C (green), 1I (blue), and 1G (orange). The solid lines are quadratic fits to the cross-correlation curves. Cross symbols mark the location of maximum correlation and corresponding lag.

of $2.6 \times 10^3\, e^-/\mathrm{cm}^2/\mathrm{s}$ for electron energies between 1.34 MeV and 1.36 MeV. Electron fluxes for duskside relativistic band precipitation can vary dependent on radiation belt electron populations and energy-dependent precipitation mechanisms. *Blum et al.* [2013] reported electron fluxes from duskside relativistic band precipitation observed by the Colorado Student Space Weather Experiment (CSSWE) on 18 January 2013 in conjunction with BARREL X-ray observations. There were two bands of precipitation during this time period of which instrumentation on board the CSSWE satellite measured different fluxes of $\sim 5.0 \times 10^4\, e^-/\mathrm{cm}^2\,\mathrm{s}$ and $\sim 1.6 \times 10^4\, e^-/\mathrm{cm}^2\,\mathrm{s}$ over an energy range of 0.58 MeV to 3.8 MeV [*Blum et al.*, 2013]. The BARREL electron fluxes we present here as observed on the following day are approximately an order of magnitude less than the CSSWE observations. However, these results are approximated for a much narrower energy range and during a time period when the radiation belts were already depleted from precipitation events the previous day. It seems reasonable to expect that whatever precipitation mechanism is driving these events would result in a range of observed precipitating electron fluxes. Depending on the estimated size of the region of precipitation and the duration of individual events, these observed events can represent the loss of a significant portion of the electron population in a radiation belt drift shell orbit.

3.2. Timing Analysis: Gamma Ray Burst

One of the advantages to having an array of observations such as BARREL is the opportunity to investigate temporal features in the data. As mentioned earlier, many of the individual events observed showed different time scale modulation in the X-ray observations. Timing accuracy can become important, particularly when studying short bursty events such as microbursts with structure on ~100 ms time scales. BARREL data are associated with a frame counter produced by an onboard clock which is not temperature controlled. Furthermore, GPS data are recorded every 4 s with GPS pulse per second (PPS) with 1 ms accuracy recorded every second. A time model is developed using frame number, GPS-recorded time, and GPS PPS data to construct a time stamp for each measurement with accuracy near 1 ms.

Another means for studying temporal features in the data is considering the timing of events between payloads. Here timing information is important when attempting to correlate precipitation events to satellite observations in order to test theories for precipitation mechanisms. The BARREL FSPC time resolution is 50 ms. The timing accuracy can be verified using the BARREL observations of gamma ray bursts (GRBs) and comparing them to an independent observation. Gamma ray bursts are pulses of gamma rays emitted from extremely energetic explosions from distance galaxies. These pulses can last hundreds of milliseconds (short bursts) to several seconds (long bursts) and are accompanied by X-rays which often host the peak energy flux at a few hundred keV [*Piran*, 2004]. There is good agreement between the observed signal by the Fermi satellite and the temporal features observed by BARREL for the GRB observed on 21 January 2013 (see Figure 8). A cross correlation of the GRB observation and the BARREL payloads tests the timing accuracy of each payload as well as the interpayload timing. Figure 10 shows cross correlation of each payload's FSPC 1 data with Fermi GBM observations. The FSPC 1 data were used in this analysis as it contains fractionally lower background counts to GRB signal in comparison to the higher-energy binned data, FSPC 2–4. For the various payloads, different cross-correlation peak values are explained by the different strengths of the observed GRB signal relative to the different cosmic ray backgrounds. For example, payload 1I at 24 km altitude has the lowest correlation due to low signal-to-noise ratio from added atmospheric attenuation when compared to the other payloads at altitudes above 30 km. To estimate the

uncertainty in the cross-correlation values, we assumed that the observed counts are distributed as Poisson random variables and then propagate count uncertainties through the cross-correlation calculation. This uncertainty is shown in Figure 10 as vertical error bars on each point. A quadratic is fit to each cross-correlation curve in order to determine the lag of maximum correlation. Figure 10 shows the location of the lag for the maximum cross correlation taking into account the error in the cross-correlation calculation and error in the quadratic fit to the cross-correlation data. The lag of maximum cross correlation for those payloads with minimum noise, 1H, 1C, 1Q, and 1G, is less than 100 ms (Figure 10). The calculated uncertainty in the location of these peaks is approximately 50 ms. The relative location of each maximum correlation suggests that the BARREL interpayload timing is also accurate and near the time resolution of the FSPC data.

4. Discussion and Conclusions

The BARREL observations on 26 January 2013 showed a range of temporal structure varying from tens of minutes or drift echo time scales to the very fast microburst time scales at fractions of seconds. Previous balloon observations have also detected X-ray count rate modulation with drift time scales but did not have the relevant satellite data to confirm that drift echoes were present in the magnetosphere. Future studies will look more closely at this specific event to determine if the chorus waves observed by Van Allen Probes could pitch angle scatter local radiation belt electrons to produce the microbursts observed at BARREL. These observations in particular are of interest as we see precipitation on multiple time scales and with features consistent with different loss processes. This event can test multiple wave-particle loss mechanisms and their respective effect on radiation belt loss.

ULF waves have been commonly linked to acceleration of radiation belt particles. A recent modeling study looked at ULF modulation of relativistic electron precipitation from MINIS balloon campaign 2005 X-ray observations and suggested that relativistic electrons could be precipitated by ULF waves [*Brito et al.*, 2012]. Multiple precipitation events observed by BARREL showed oscillations in the X-ray count rate at ULF time scales (Pc3–Pc5). Two such events were shown here with observations from 26 January 2013 and 19 January 2013. Both events have very different energy spectra with the 19 January 2013 observations extending up to relativistic electron energies. Additional information provided by other ground-based instruments and satellites, such as Halley VI, GOES, and Van Allen Probes, in conjunction with the balloons can help determine if ULF waves are precipitating the particles or modulating the loss process that scatters the particles into the loss cone.

Duskside relativistic electron precipitation has often been attributed to scattering by EMIC waves [*Usanova et al.*, 2014; *Miyoshi et al.*, 2008; *Lorentzen et al.*, 2000]. Ground-based magnetometer data at Halley VI station, Antarctica, show that EMIC waves were present just prior to the relativistic event observed by BARREL payload 1H on 19 January 2013. Modeled precipitating electron distributions suggest that this event is characterized by a peaked distribution suggesting an energy selective precipitation mechanism which is consistent with precipitation from pitch angle scattering by EMIC waves [*Ukhorskiy et al.*, 2010; *Miyoshi et al.*, 2008; *Meredith et al.*, 2003; *Lorentzen et al.*, 2000]. Using data from Van Allen Probes and GOES will help to determine if the presence of EMIC waves with the observed precipitation is causation or correlation.

A gamma ray burst was observed by BARREL payloads above 20 km on 21 January 2013. The observed gamma ray burst provided a timing strobe that was used to independently study the BARREL timing system. The result of the study was agreement between BARREL and Fermi timing systems to within a BARREL sampling interval of 0.05 s. Good timing accuracy is important when studying events with high time resolution structure like microburst, when trying to investigate temporal features in observations between payloads, as well as when trying to correlate precipitation observations to satellite wave data.

The BARREL team had two balloon campaigns throughout the Antarctic summers of 2013 and 2014, during which precipitation was observed over a wide range of energy, time scales, and spatial scales. Precipitation occurred during a variety of magnetospheric conditions with many instances of good conjunctions with the Van Allen Space Probes. Microburst precipitation and duskside relativistic electron precipitation were observed by BARREL balloons during both campaigns. The array of balloons allows for the exploration of

temporal and spatial variations of precipitation events [e.g., *Blum et al.*, 2013]. This data set provides valuable observations of radiation belt electron losses which contribute to the extreme variability of radiation belt particle fluxes.

Acknowledgments
The authors acknowledge NASA grant NNX08AM58G and the BARREL team for the use of BARREL data. BARREL data used in this paper can be obtained through the SPEDAS software package as well as at CDAWeb website. The authors would like to thank the National Environmental Research Council/British Antarctic Survey and the South African National Antarctic Program for their support and collaboration during the BARREL balloon campaigns. We acknowledge the Fermi mission for the use of their data specifically the GBM instrument (http://heasarc.gsfc.nasa.gov/FTP/fermi/data/gbm). MagEIS efforts are supported by Van Allen Probe-ECT funding provided by JHU/APL contract 967399. We acknowledge the use of NASA/GSFC's Space Physics Data Facility's OMNIWeb (or CDAWeb) service and OMNI data.

References

Anderson, B. J., R. E. Erlandson, and L. J. Zanetti (1992), A statistical study of Pc1–2 magnetic pulsations in the equatorial magnetosphere: 2. Wave properties, *J. Geophys. Res.*, *97*(A3), 3075–3101, doi:10.1029/91JA02706.

Anderson, K. A., and D. W. Milton (1964), Balloon observations of X-rays in the auroral zone: 3. High time resolution studies, *J. Geophys. Res.*, *69*(21), 4457–4479, doi:10.1029/JZ069i021p04457.

Baker, D. N. (1996), Solar wind-magnetosphere drivers of space weather, *J. Atmos. Sol. Terr. Phys.*, *58*, 1509–1526.

Berger, M. J., and S. M. Seltzer (1972), Bremsstrahlung in the atmosphere, *J. Atmos. Sol. Terr. Phys.*, *34*, 85–108.

Blake, J. B., M. D. Looper, D. N. Baker, R. Nakamura, B. Klecker, and D. Hovestadt (1996), New high temporal and spatial resolution measurements by SAMPEX of the precipitation of relativistic electrons, *Adv. Space Res.*, *18*(8), 171–186.

Blum, L. W., Q. Schiller, X. Li, R. Millan, A. Halford, and L. Woodger (2013), New conjunctive CubeSat and balloon measurements to quantify rapid energetic electron precipiation, *Geophys. Res. Lett.*, *40*, 5833–5837, doi:10.1002/2013GL058546.

Brito, T., L. Woodger, M. Hudson, and R. Millan (2012), Energetic radiation belt electron precipiation showing ULF modulation, *Geophys. Res. Lett.*, *39*, L22104, doi:10.1029/2012GL053790.

Brown, J. W., and E. C. Stone (1972), High-energy electron spikes at high latitudes, *J. Geophys. Res.*, *77*(19), 3384–3396, doi:10.1029/JA077i019p03384.

Callis, L. B., R. E. Boughner, D. N. Baker, R. A. Mewaldt, J. Bernard Blake, R. S. Selesnick, J. R. Cummings, M. Natarajan, G. M. Mason, and J. E. Mazur (1996), Precipitating electrons: Evidence for effects on mesospheric odd nitrogen, *Geophys. Res. Lett.*, *23*(15), 1901–1904, doi:10.1029/96GL01787.

Clilverd, M. A., A. Seppala, C. J. Rodger, M. G. Mlynczak, and J. U. Kozyra (2009), Additional stratospheric NO_x production by relativistic electron precipitation during the 2004 spring NO_x descent event, *J. Geophys. Res.*, *114*, A04305, doi:10.1029/2008JA013472.

Clilverd, M. A., C. J. Rodger, D. Danskin, M. E. Usanova, T. Raita, T. Ulich, and E. L. Spanswick (2012), Energetic particle injection, acceleration, and loss druing the geomagnetic disturbances which upset Galaxy 15, *J. Geophys. Res.*, *117*, A12213, doi:10.1029/2012JA018175.

Comess, M. D., D. M. Smith, R. S. Selesnick, R. M. Millan, and J. G. Sample (2013), Duskside relativistic electron precipitation as measured by SAMPEX: A statistical study, *J. Geophys. Res. Space Physics*, *118*, 5050–5058, doi:10.1002/jgra.50481.

Foat, J. E., et al. (1998), First detection of a terrestrial MeV X-ray burst, *Geophys. Res. Lett.*, *25*(22), 4109–4112, doi:10.1029/1998GL900134.

Green, J. C., T. G. Onsager, T. P. O'Brien, and D. N. Baker (2004), Testing loss mechanisms capable of rapidly depleting relativistic electron flux in the Earth's outer radiation belt, *J. Geophys. Res.*, *109*, A12211, doi:10.1029/2004JA010579.

Halford, A. J., et al. (2015), BARREL observations of an ICME-shock impact with the magnetosphere and the resultant radiation belt electron loss, *J. Geophys. Res. Space Physics*, *120*, doi:10.1002/2014JA020873.

Hudson, M. K., D. N. Baker, J. Goldstein, B. T. Kress, J. Paral, F. R. Toffoletto, and M. Wiltberger (2014), Simulated magnetopause losses and Van Allen Probe flux dropouts, *Geophys. Res. Lett.*, *41*, 1113–1118, doi:10.1002/2014GL059222.

Imhof, W. L., H. D. Voss, J. B. Reagan, D. W. Datlowe, E. E. Gaines, J. Mobilia, and D. S. Evans (1986), Relativistic electron and energetic ion precipitation spikes near the plasmapause, *J. Geophys. Res.*, *91*(A3), 3077–3088, doi:10.1029/JA091iA03p03077.

Imhof, W. L., H. D. Voss, J. Mobilia, D. W. Datlowe, E. E. Gaines, J. P. McGlennon, and U. S. Inan (1992), Relativsitic electron microbursts, *J. Geophys. Res.*, *97*(A9), 13,829–13,837, doi:10.1029/92JA01138.

Li, Z., et al. (2014), Investigation of EMIC wave scattering as the cause for the BARREL 17 January 2013 relativistic electron precipitation event: A quantitative comparison of simulation with observation, *Geophys. Res. Lett.*, *41*, 8722–8729, doi:10.1002/2014GL062273.

Lorentzen, K. R., M. P. McCarthy, G. K. Parks, J. E. Foat, R. M. Millan, D. M. Smith, R. P. Lin, and J. P. Treilhou (2000), Precipitation of relativistic electrons by interaction with electromagnetic ion cyclotron waves, *J. Geophys. Res.*, *105*(A3), 5381–5390, doi:10.1029/1999JA000283.

Lorentzen, K. R., J. B. Blake, U. S. Inan, and J. Bortnik (2001), Observations of relativistic electron microbursts in association with VLF chorus, *J. Geophys. Res.*, *106*(A4), 6017–6028, doi:10.1029/2000JA003018.

Mauk, B. H., N. J. Fox, S. G. Kanekal, R. L. Kessel, D. G. Sibeck, and A. Ukhorskiy (2013), Science objectives and rationale for the radiation storm probes mission, *Space Sci. Rev.*, *179*, 3–27.

Meegan, C. A., et al. (2009), The Fermi Gamma-ray Burst Monitor, *Astrophys. J.*, *702*(1), 791–804.

Meredith, N. P., R. M. Thorne, R. B. Horne, D. Summers, B. J. Fraser, and R. R. Anderson (2003), Statistical analysis of relativistic electron energies for cyclotron resonance with EMIC waves observed on CRRES, *J. Geophys. Res.*, *108*(A6), 1250, doi:10.1029/2002JA009700.

Millan, R. M., and BARREL Team (2011), Understanding relativistic electron losses with BARREL, *J. Atmos. Sol. Terr. Phys.*, *73*(11–12), 1425–1434.

Millan, R. M., and R. M. Thorne (2007), Review of radiation belt relativistic electron losses, *J. Atmos. Sol. Terr. Phys.*, *69*(3), 362–377.

Millan, R. M., R. P. Lin, D. M. Smith, K. R. Lorentzen, and M. P. McCarthy (2002), X-ray observations of MeV electron precipitation with a balloon-borne germanium spectrometer, *Geophys Res. Lett.*, *29*(24), 47–1, doi:10.1029/2002GL015922.

Millan, R. M., R. P. Lin, D. M. Smith, and M. P. McCarthy (2007), Observation of relativistic electron precipitation during a rapid decrease of trapped relativistic electron flux, *Geophys. Res. Lett.*, *34,* L10101, doi:10.1029/2006GL028653.

Millan, R. M., K. B. Yando, J. C. Green, and A. Y. Ukhorskiy (2010), Spatial distribution of relativistic electron precipitation during a radiation belt depletion event, *Geophys. Res. Lett.*, *37*, L20103, doi:10.1029/2010GL044919.

Millan, R. M., et al. (2013), The Balloon Array for RBSP Relativistic Electron Losses (BARREL), *Space Sci. Rev.*, *179*(1–4), 503–530.

Miyoshi, Y., K. Sakaguchi, K. Shiokawa, D. Evans, J. Albert, M. Connors, and V. Jordanova (2008), Precipitation of radiation belt electrons by EMIC waves, observed from ground and space, *Geophys. Res. Lett.*, *35*, L23101, doi:10.1029/2008GL035727.

O'Brien, T. P., M. D. Looper, and J. B. Blake (2004), Quantification of relativistic electron microburst losses during the GEM storms, *Geophys. Res. Lett.*, *31*, L04802, doi:10.1029/2003GL018621.

Piran, T. (2004), The physics of gamma-ray bursts, *Rev. Mod. Phys.*, *76*(4), 1143–1210.

Reeves, G. D., K. L. McAdams, R. H. Friedel, and T. P. O'Brien (2003), Acceleration and loss of relativistic electrons during geomagnetic, *Geophys. Res. Lett.*, *30*(10), 1529, doi:10.1029/2002GL016513.

Rosenberg, T. J., R. Wei, D. L. Detrick, and U. S. Inan (1990), Observations and modeling of wave-induced microbursts electron precipitation, *J. Geophys. Res.*, *95*, 6467–6475, doi:10.1029/JA095iA05p06467.

Sazhin, S. S., and M. Hayakawa (1992), Magnetospheric chorus emissions: A review, *Planet. Space Sci.*, *40*(No5), 681–697.

Thorne, R. M. (2010), Radiation belt dynamics: The importance of wave particle interactions, *Geophys. Res. Lett.*, *37*, L22107, doi:10.1029/2010GL044990.

Thorne, R. M., and C. F. Kennel (1971), Relativistic electron precipitation during magnetic storm main phase, *J. Geophys. Res.*, *76*(19), 4446–4453, doi:10.1029/JA076i019p04446.

Turner, D. L., Y. Shprits, M. Hartinger, and V. Angelopoulos (2012), Explaining sudden losses of outer radiation belt electrons during geomagnetic storms, *Nat. Phys.*, *8*(3), 208–2012.

Ukhorskiy, A. Y., B. J. Anderson, P. C. Brandt, and N. A. Tsyganenko (2006), Storm time evolution of the outer radiation belt: Transport and losses, *J. Geophys. Res.*, *111*, A11S03, doi:10.1029/2006JA011690.

Ukhorskiy, A. Y., Y. Y. Shprits, B. J. Anderson, K. Takahashi, and R. M. Thorne (2010), Rapid scattering of radiation belt electrons by storm-time EMIC waves, *Geophys. Res. Lett.*, *37*, L09101, doi:10.1029/2010GL042906.

Usanova, M. E., et al. (2014), Effect on EMIC waves on relativistic and ultrarelativistic electron populations: Ground-based and Van Allen Probes observations, *Geophys. Res. Lett.*, *41*, 1375–1381, doi:10.1002/2013GL059024.